Final Draft
of the original manuscript:

Winzer, N.; Atrens, A.; Dietzel, W.; Song, G.; Kainer, K.U.:
Stress Corrosion Cracking (SCC) in Mg-Al Alloys Studied using Compact Specimens
In: Advanced Engineering Materials (2008) Wiley

DOI: 10.1002/adem.200700319

Stress Corrosion Cracking (SCC) in Mg-Al Alloys Studied using Compact Specimens

N. Winzer[a], A. Atrens[a,b], W. Dietzel[c], G. Song[a], K.U. Kainer[c]

[a] Materials Engineering, The University of Queensland, Brisbane 4072, Australia

Email: nickwinz@graduate.uwa.edu.au

Phone: +49(0)15201363229

[b] Swiss Federal Laboratories for Materials Science and Technology, EMPA, Dept 136, Überlandstrasse 129, CH-8600 Dubendorf, Switzerland

[c] Institute for Materials Research, GKSS-Forschungszentrum Geesthacht GmbH, D-21502, Geesthacht, Germany

Keywords: magnesium; stress corrosion cracking; hydrogen embrittlement; compact specimens; linearly increasing stress test; crack velocity measurement.

Abstract

Stress Corrosion Cracking (SCC) of the Mg-Al alloys AZ91 and AZ31 was studied using compact, or C(T), specimens. For AZ31, the stress corrosion crack velocity, V_c, was in the range 2.5×10^{-9} – 8×10^{-9} m/s, and the threshold stress intensity factor, K_{ISCC}, was ~13.7 MPa√m. The fracture surfaces for AZ31 contained cleavage-like facets similar to those observed on SCC fracture surfaces for AZ31 and AZ91 cylindrical tensile specimens; however, the cleavage-like facets did not appear to contain micro-dimples as observed for the cylindrical tensile specimens. SCC in AZ91 C(T) specimens was characterised by superficial stress corrosion crack branches extending from the fatigue crack tip along the maximum principle stress contours in the region

where the maximum principle stress exceeded σ_{SCC}. The absence of a primary stress corrosion crack through the entire width of the specimen prevented V_c and K_{ISCC} from being measured for AZ91.

1 Introduction

Our recent publications [1, 2, 3, 4, 5, 6, 7] showed that there exists a considerable body of research outlining the phenomenology of Transgranular Stress Corrosion Cracking (TGSCC) in Mg alloys. TGSCC is the inherent mode of SCC in Mg alloys. It is generally accepted that the mechanism for TGSCC of Mg alloys is a form of Hydrogen Embrittlement (HE) with the hydrogen coming from the cathodic partial reaction (hydrogen generation) of the Mg corrosion reaction [8, 9, 10, 11]; however, the specific nature of the HE mechanism remains uncertain. The mechanisms that have been proposed are: Hydrogen Enhanced Decohesion (HEDE) [2]; Hydrogen Enhanced Localised Plasticity (HELP) [2]; Adsorption Induced Dislocation Emission (AIDE) [12]; and Delayed Hydride Cracking (DHC) [7, 13, 14, 15, 16].

Determination of the mechanism for TGSCC of Mg alloys is complicated by its dependence on microstructure, environment and mechanical loading. A key indicator of the predominant mechanism for an SCC system is the stress corrosion crack velocity, V_c. AIDE involves enhanced microvoid coalescence due to emission of dislocations from the crack tip by adsorbed H atoms. Since AIDE does not involve transport of H into the matrix, it is associated with very high V_cs [12, 17, 18]. HELP involves enhanced dislocation mobility due to H atmospheres at dislocations and obstacles to dislocations. Thus, HELP is associated with moderate V_cs, at which H atmospheres can remain bound to mobile dislocations [18, 19]. HEDE and DHC involve stress-assisted

diffusion of H ahead of the crack tip, which is slower than H transport by mobile dislocations (as per HELP) [20]. Thus, HEDE and DHC are associated with relatively low V_cs.

2 Experimental Method

C(T) specimens were machined from the Mg-Al alloys AZ91 and AZ31. These alloys were the same as those used (in the form of cylindrical tensile specimens) in our previous research [2, 3, 6]. AZ91 consisted of an α-matrix with an extensive interdendritic β-phase, whereas AZ31 consisted of an α-matrix with Al-concentration similar to that in AZ91. AZ91 specimens were machined from as-cast ingots, whereas AZ31 specimens were machined from large extrusions such that the crack propagation direction was parallel with the extrusion direction. The specimens were 7.5 mm thick and were fatigue pre-cracked such that $a/W \approx 0.5$ (where W is 40 mm) at the beginning of each SCC test. The SCC test environment was double-distilled H_20. Control tests were carried out in laboratory air (previously shown to be inert [2, 3, 6]). The experimental setup for SCC tests is shown in Figure 1. The specimens were immersed in the environment to just above the machined notch. The fatigue crack was saturated with distilled water prior to each test by applying a small constant load (~0.5 kN) to the immersed specimen for ~24 h. The distilled water was slowly circulated between the environment cell and a remote reservoir. The applied tensile load was increased under Constant Extension Rate Test (CERT) conditions, with the extension measured using a clip gauge at the crack mouth. The extension rates used were 2 μm/h for AZ31 and 2 – 16 μm/h for AZ91. Stress corrosion crack propagation was measured using the pulsed DCPD method as described in our previous publications [2, 3, 6].

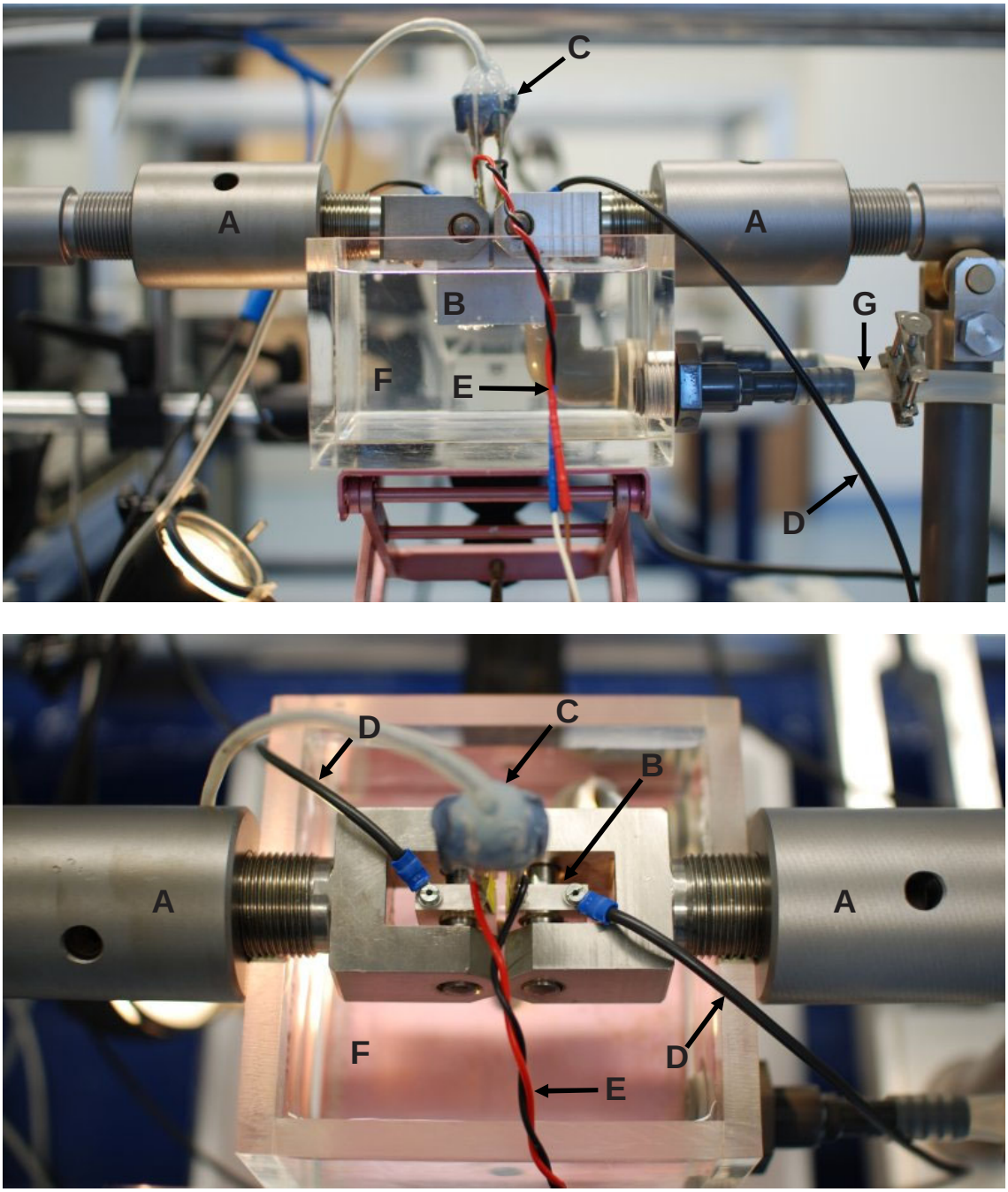

Figure 1 – Experimental setup showing: (A) load train; (B) specimen; (C) clip gauge; (D) current leads; (E) voltage probes; (F) environment cell; and (G) environment feed from reservoir.

3 Results

SCC occurred in AZ91 and AZ31; however, the morphologies of the stress corrosion cracks in AZ91 and AZ31 were in stark contrast. For AZ31, there was a single stress

corrosion crack extending from the tip of the fatigue crack, through the entire width of the specimen, and propagating perpendicular to the loading direction. For AZ91, there were multiple superficial stress corrosion cracks branching from the fatigue crack tip along the maximum principle stress contours (see Section 3.3).

3.1 SCC of AZ31

Figures 2 and 3 show the mechanical load versus crack opening displacement (COD) and DCPD versus COD curves respectively for AZ31 in distilled water and laboratory air. In laboratory air, there was no crack extension until COD > 5 mm, after which there was a reduction in engineering stress with crack propagation. COD was measured up to 9.5 mm; however, Figures 2 – 3 show only COD ≤ 1.2 mm. K_{IC} was calculated from the initial crack length and the load corresponding to crack initiation as 31.7 MPa√m.

For specimens in distilled water, the ultimate mechanical load was 60% lower, and occurred at a much lower COD, relative to specimens in laboratory air. The initial section of the DCPD versus COD curve (i.e. COD < 0.48 mm) was characterised by a small, constant and positive gradient, which may indicate changes in the specimen geometry in the vicinity of the crack tip (i.e. due to crack tip blunting and plastic zone development). The initial gradient of the mechanical load versus COD curve for distilled water was considerably less than that for laboratory air, indicating that the crack tip stress field is influenced by loading in distilled water.

For specimens in distilled water, the apparent plastic deformation (see Figure 2) is mostly attributed to stress corrosion crack propagation. The onset of apparent plastic deformation (i.e. at COD ≈ 0.48 mm) corresponded with a sharp increase in the gradient of the DCPD curve. Thus, the threshold stress intensity, K_{ISCC}, was interpreted as the

stress intensity factor corresponding to this increase in the gradient of the DCPD curve. K_{ISCC} was calculated from the initial crack length and load at SCC initiation to be ~13.7 MPa√m. Stress corrosion crack propagation beyond K_{ISCC} eventually resulted in a reduction in the mechanical load. The test was eventually interrupted and the remaining ligament fractured under a high strain rate in laboratory air.

The stress corrosion crack velocity was calculated from the DCPD measurements using the equation:

$$\frac{V_1}{V_2} = \frac{A_2}{A_1} \qquad \text{Equation 1}$$

where V_1 and V_2 are the temperature-corrected DCPD measurements, and A_1 and A_2 the cross-sectional areas of the specimen in the crack plane, at the beginning and end of the test respectively. The final stress corrosion crack length calculated using Equation 1 was 66 % smaller than the average final crack length measured on the fracture surface. This difference was attributed to the conductance of the environment between the opposing crack surfaces. Assuming that the conductance of the environment remained constant throughout the test, the calculated stress corrosion crack lengths corresponding to each DCPD measurement were scaled such that the calculated final crack length was equal to the measured value. Figure 4 shows the stress corrosion crack velocity (*da/dt*) versus K_I curve (for $K_I > K_{ISCC}$) for AZ31 in distilled water. K_I was calculated from the DCPD-furnished crack lengths. *da/dt* was calculated by differentiating a 3rd order polynomial fitted to the *a* versus *t* curve. Figure 4 shows that *da/dt* increased towards an asymptote of ~8x10^{-9} m/s.

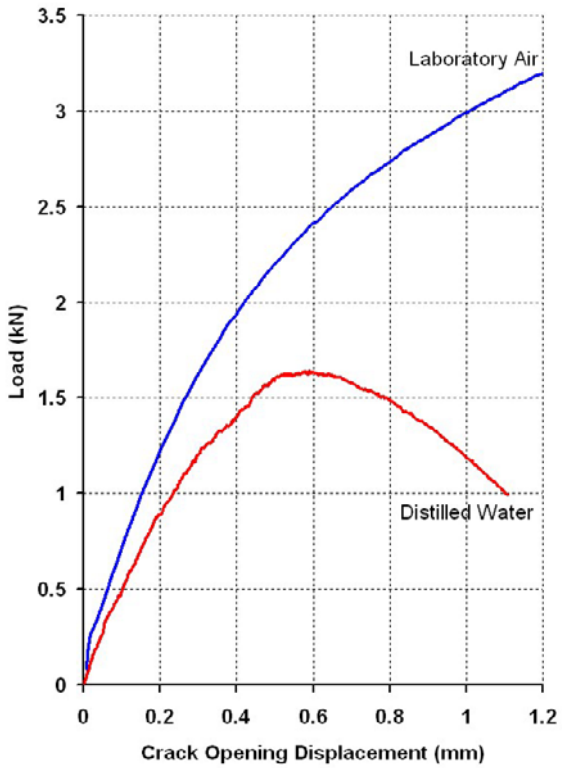

Figure 2 – Mechanical load versus crack opening displacement curve for AZ31 CT specimen tested in distilled water at 2 μm/h.

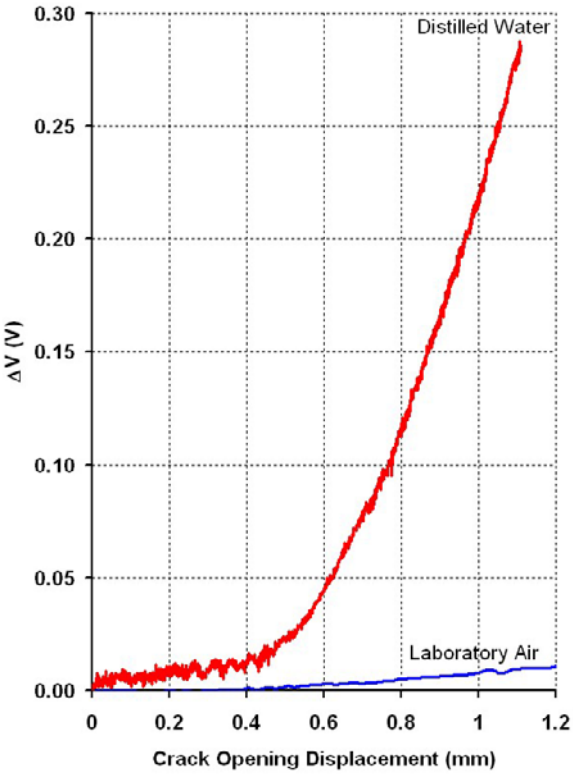

Figure 3 – DCPD signal (ΔV) versus crack opening displacement curve for AZ31 CT specimen tested in distilled water at 2 μm/h.

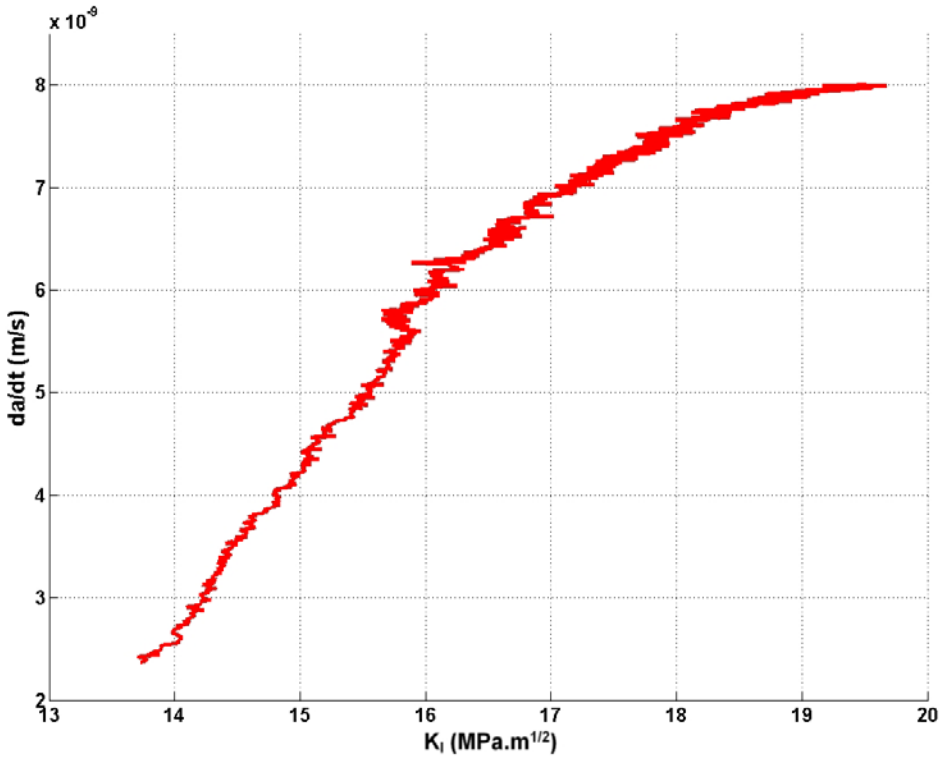

Figure 4 – Crack velocity (da/dt) versus K_I curve for AZ31 CT specimen tested in distilled water at 2 μm/h.

3.2 AZ31 Fractography

The fracture surfaces for AZ31 in distilled water consisted of three distinctly different zones corresponding to: (i) fatigue; (ii) SCC and (iii) final overload fracture (see Figure 5). The SCC zone was characterised by: (i) regions containing smooth rounded features (left side of Figure 6A); (ii) regions containing cleavage-like features (see Figures 6B – F); and (iii) extensive secondary crack branching (see Figure 6A). The cleavage-like features were similar to those observed on SCC fracture surfaces for AZ91 cylindrical tensile specimens, but were more characteristically cleavage-like than those observed on SCC fracture surfaces for AZ31 cylindrical tensile specimens [2]. The cleavage-like facets were aligned in the direction of crack propagation, and sometimes contained fine parallel markings 1 – 2 μm apart (see Figure 6C); however, they did not contain micro-dimples as observed on SCC fracture surfaces for AZ91 and AZ31 cylindrical tensile specimens [2]. The final overload fracture zone was characterised by coarse, irregular dimple-like features (see Figures 6G – 6H), consistent with fracture surfaces produced in air [2]. The final overload fracture zone also contained 45° shear lips and deformation in the thickness direction, consistent with the development of a large plastic zone at the crack tip.

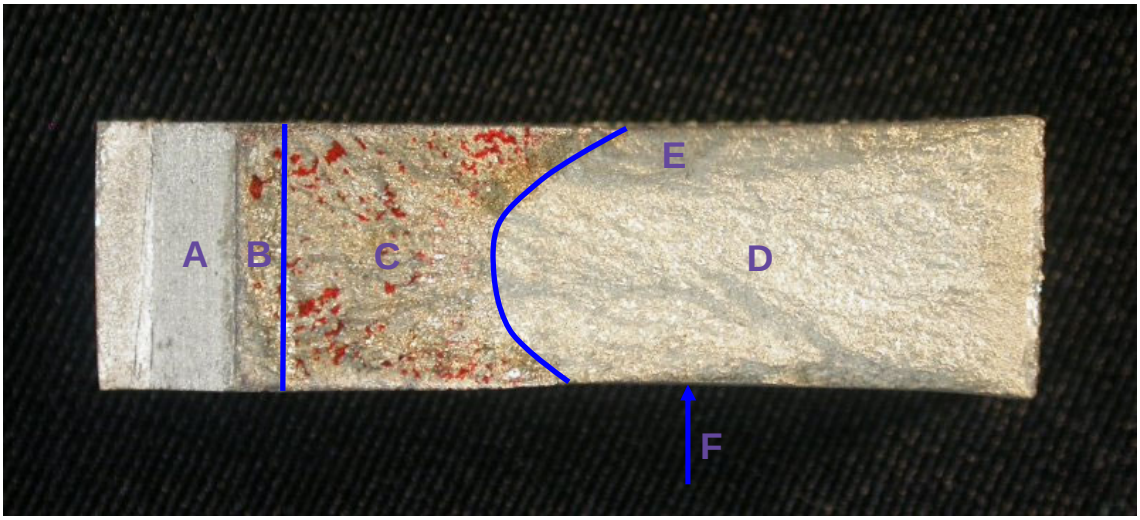

Figure 5 – Overview of fracture surface for AZ31 CT specimen tested in distilled water at 2 μm/h showing: (A) machined notch; (B) fatigue pre-cracked zone; (C) SCC zone; (D) final fracture zone; (E) shear lips; and (F) deformation in the thickness direction. The red patches are due to dye penetrant marking of the SCC zone before final fracture.

3.3 Surface Cracking in AZ91

For AZ91 in distilled water, SCC was manifested by superficial crack branches of depth < 1 mm extending in multiple directions from the fatigue crack tip (Figure 7), with H_2 gas bubble evolution occurring within the crack branches (Figure 8). A detailed view of a typical crack branch is given in Figure 9. The crack branches occurred within the region where the maximum principal stress was greater than the threshold stress for SCC, σ_{SCC}. Since the specimens were in the plane stress state, the maximum principal stress is given by:

$$\sigma_1 = \frac{K_I}{\sqrt{2\pi r}} \cos\left(\frac{\theta}{2}\right)\left[1+\sin\left(\frac{\theta}{2}\right)\right] \qquad \text{Equation 2}$$

where K_I is the crack tip stress intensity factor and r is the radius from the crack tip. Thus, the boundary of the region containing crack branches is calculated by substituting σ_{SCC} for σ_1. Figure 10 shows the SCC zone boundary assuming $\sigma_{SCC} \approx 60$ MPa [3, 6] and $K_I = 14$ MPa/m$^{1/2}$ (calculated from the initial crack length and the load

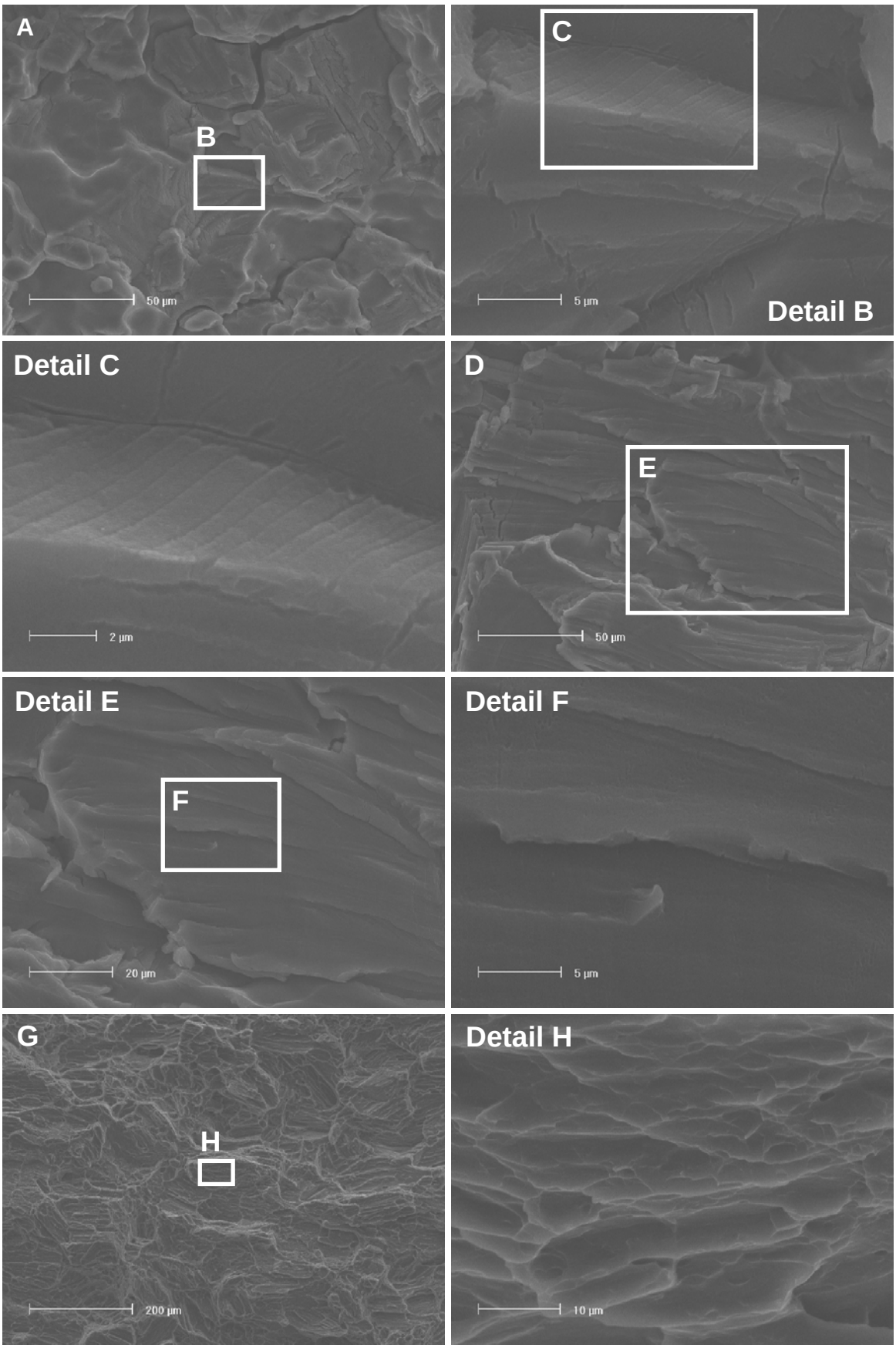

Figure 6 – SEM fractographs for AZ31 specimen tested in distilled water at 2 µm/h.

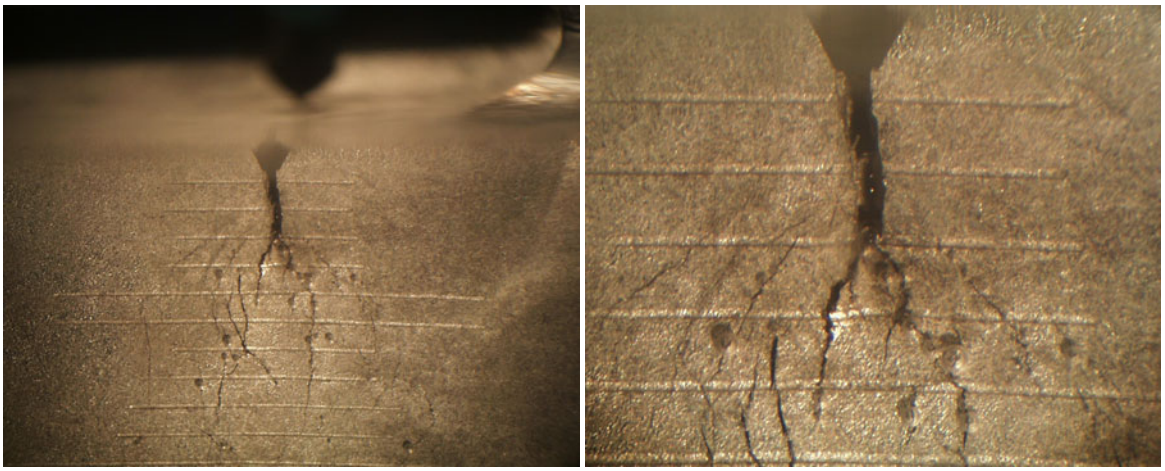

Figure 7 – Secondary crack branching for AZ91 CT specimen tested in distilled water.

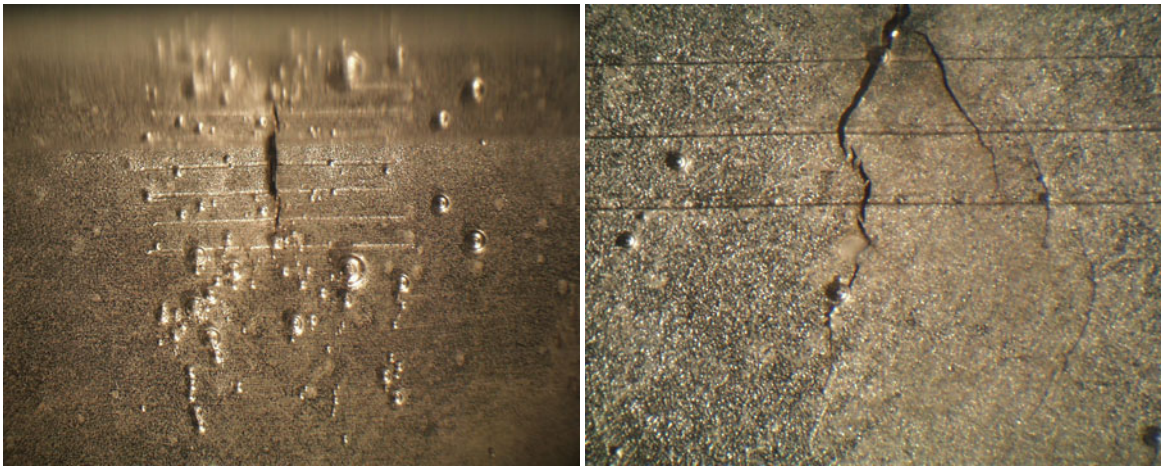

Figure 8 – H_2 bubbles within stress corrosion cracks for AZ91 CT specimen tested in distilled water.

corresponding to crack initiation). The crack branches are invariably oriented parallel with the SCC zone radius (or the contours of the maximum principal stress). Figure 10 also shows the plastic zone radius for inert conditions (assuming K_I = 14 MPa/m$^{1/2}$ and σ_Y = 110 MPa [7]); however, this is for reference only since the plastic zone varies considerably due to the SCC mechanism. Figure 11 shows the plastic zone (visible as deformation in the thickness direction) at the crack tip for AZ91 specimens tested in laboratory air.

Figure 9 – Surface secondary cracking in AZ91 CT specimen tested in distilled water.

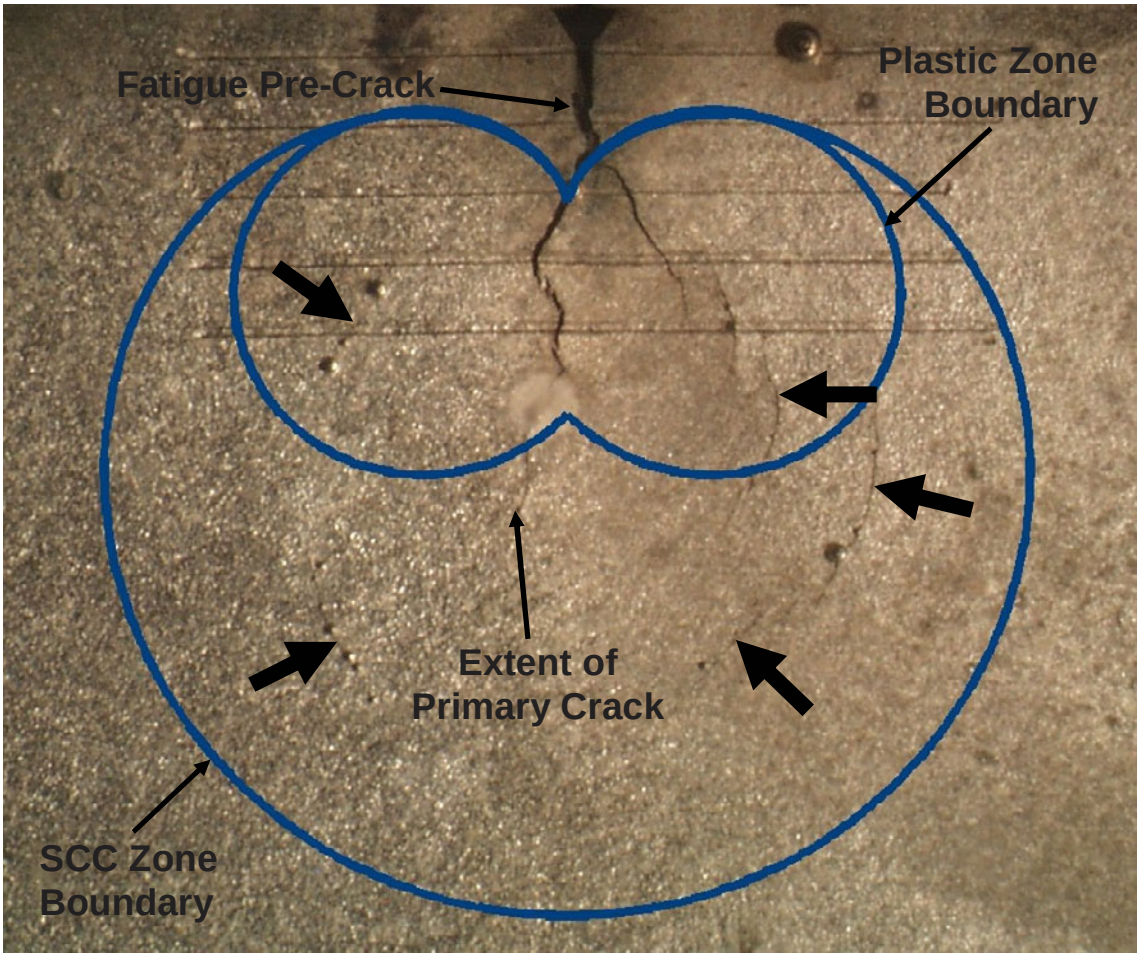

Figure 10 – "Radial" secondary cracks (indicated by large arrows) within the boundaries defined by Tresca criteria using σ_{SCC} = 60 MPa and σ_Y = 110 MPa.

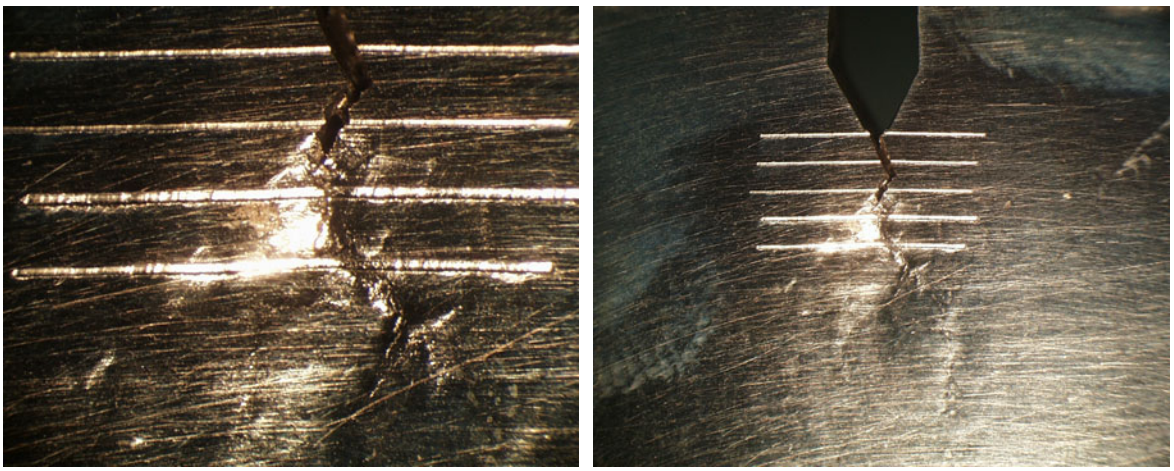

Figure 11 – Plastic zone ahead of a crack tip for a CT specimen fractured in air.

4 Discussion

The initial gradient of the mechanical load versus COD curve for AZ31 in distilled water was considerably less than that for laboratory air, indicating that the crack tip stress field is influenced by the SCC mechanism. The reduction in the gradient of the mechanical load versus COD curve in the presence of distilled water is consistent with an increase in the plastic zone size, even though the SCC fracture surface morphology was indicative of HE and there was no visible plastic deformation on plane surface of the specimen. Previous workers [21, 22, 23, 24] have measured significant increases in plastic zone size for high-strength steels in the presence of cathodically produced or gaseous H. This phenomenon has been attributed to the influence of H on the mobility of dislocations in the plastic zone (as per HELP) [25].

The K_{ISCC} value determined from the DCPD measurements for AZ31 (~13.7 MPa√m) was in the upper range of values given by previous workers for Mg alloys [26, 27, 28]. Stephens et al [26] measured K_{ISCC} = 7.5 MPa√m for cast AZ91 in NaCl solution. Speidel et al [27] measured K_{ISCC} = 12 MPa√m in distilled water, K_{ISCC} = 8 MPa√m in Na_2SO_4 solution and K_{ISCC} = 5 MPa√m in NaBr solution for the Mg alloy ZK60A-T5. Ebtehaj et al [28] measured K_{ISCC} = 7 – 14 MPa√m for Mg-9Al in solutions containing various ratios of NaCl and K_2CrO_4, with the minimum K_{ISCC} occurring at intermediate ratios. NaCl and K_2CrO_4 are generally associated with surface film breakdown and repassivation respectively [16, 28]. Thus, K_{ISCC} is dependent on the propensity for film breakdown and H ingress at the crack tip. The Mg-9Al alloy used by Ebtehaj et al [28] is likely to have had a similar α-phase composition to the AZ31 alloy used in the present research. Thus, given that distilled water does not promote localised corrosion in AZ31 [6], this implies that the measured K_{ISCC} is not the minimum value

for AZ31, and that it may be reduced by using a slightly more aggressive environment (e.g. dilute NaCl solution).

The range of V_cs shown in Figure 4 are consistent with the value given by Speidel et al [26] for the Mg alloy ZK50A-T5 in distilled water, but much slower than those measured for Mg alloys in other aqueous environments [5, 15, 16, 28, 29, 30, 31] and predicted using our numerical model for DHC (~10^{-7} m/s) [7]. Figure 4 is also consistent with the average V_cs measured by Winzer et al [6] for AZ31 cylindrical tensile specimens in distilled water under CERT conditions ($1.2x10^{-9}$ – $6.7x10^{-9}$ m/s), which were calculated from the width of the SCC fracture surface zone and the time from SCC initiation until test cessation [6]. The V_cs for the AZ31 cylindrical tensile specimens were associated with a mechanism involving microvoid coalescence (HELP and/or AIDE). In contrast, the V_cs for AM30 cylindrical tensile specimens were considerably slower than that for AZ31 ($3.6x10^{-10}$ – $9.3x10^{-10}$ m/s). The fracture surfaces for AM30 specimens were macroscopically similar to those for AZ31; however, there were no micro-dimples apparent at higher magnification as per AZ31. The differences in V_cs and fracture surface morphologies for AZ31 and AM30 cylindrical tensile specimens were attributed to the difference in H diffusivity in the α-matrix for the two alloys, which increases with increasing concentrations of second phase particles and Zn in solid solution with the α-matrix. It was proposed that the influence of H diffusivity on the SCC propagation mechanism may be such that: (i) different mechanisms predominate for AZ31 and AM30; or (ii) the same mechanism occurs in AZ31 and AM30, with a difference in the rate of that mechanism. In the latter case, it is possible that a reduction in H diffusivity (or the driving force for H diffusion) would also result in a reduction in the size of the micro-dimples. This may explain why

micro-dimples were not observed by SEM examination of SCC fracture surfaces for AZ31 C(T) specimens and AM30 cylindrical tensile specimens. Alternatively, the SCC fracture mode may depend on the stress state; the work of Yan et al [32] showed that the fracture of AZ91 becomes more brittle with increasing constraint.

The superficial crack branching observed for AZ91 in distilled water is ascribed to mechanical film rupture and H ingress along contours for the maximum principal stress. This implies that there is a higher propensity for mechanical film rupture and H ingress at the plane surface than at the crack tip. It is uncertain why superficial crack branching occurred for AZ91 but not AZ31, which has the same α-phase composition; however, this may be related to the role of β-phase particles (contained in AZ91 only) in crack nucleation [2, 6]. That the crack branches appear within the boundary defined by $\sigma_1 = \sigma_{SCC}$ suggests that σ_{SCC} is defined by mechanical film rupture.

5 Conclusions

- The initial gradient of the mechanical load versus COD curve for AZ31 in distilled water was considerably less than that for laboratory air. This is consistent with an increase in plastic zone size due to the influence H on the mobility of dislocations in the plastic zone (as per HELP).
- For AZ31 in distilled water, the stress corrosion crack velocity, V_c, was measured to be in the range 2.5×10^{-9} – 8×10^{-9} m/s, with V_c increasing asymptotically with increasing K_I. The threshold stress intensity factor for SCC, K_{ISCC}, was measured to be ~13.7 MPa√m.
- The fracture surfaces for AZ31 contained cleavage-like facets similar to those observed on SCC fracture surfaces for AZ31 and AZ91 cylindrical tensile specimens

[2]; however, the cleavage facets did not contain micro-dimples as were observed for AZ31 and AZ91 cylindrical tensile specimens. The contrast in fracture surfaces for C(T) and cylindrical tensile specimens could be due to a relationship between H transport in the α-matrix and the size of the micro dimples, or the higher constraint in the C(T) specimens.

- SCC in AZ91 C(T) specimens was characterised by superficial stress corrosion crack branches extending from the fatigue crack tip along the maximum principle stress contours in the region where the maximum principle stress exceeded σ_{SCC}. The absence of a primary stress corrosion crack through the entire width of the specimen prevented V_c and K_{ISCC} from being measured.

Acknowledgements

The authors wish to thank the GM Technical Centre at Warren MI, the Australian Research Council (ARC) and the Australian Research Network for Advanced Materials (ARNAM) for research support. N. Winzer and A. Atrens wish to thank GKSS Forschungszentrum Geesthacht GmbH for allowing them to visit between 2005 and 2007 and for providing research facilities. V. Heitmann, U. Burmeister and V. Kree of GKSS are thanked for their assistance with experiments, fractography and metallography.

References

[1] N. Winzer, A. Atrens, G. Song, E. Ghali, W. Dietzel, K.U. Kainer, N. Hort, C. Blawert, Adv. Eng. Mater. **2005**, 8, 659.

[2] N. Winzer, A. Atrens, W. Dietzel, G. Song, K.U. Kainer, Metall. Mater. Trans. A, article under review.

[3] N. Winzer, A. Atrens, W. Dietzel, G. Song, K.U. Kainer, Mat. Sci. Eng. A - Struct **2007**, doi:10.1016/j.msea.2007.03.021.

[4] M. Bobby Kannan, W. Dietzel, C. Blawert, A. Atrens, P. Lyon, Mat. Sci. Eng. A - Struct, **2007**, doi:10.1016/j.msea.2007.07.070.

[5] R.G. Song, C. Blawert, W. Dietzel, A. Atrens, Mater. Sci. Eng. **2005**, 399, 308.

[6] N. Winzer, A. Atrens, W. Dietzel, V.S. Raja, G. Song, K.U. Kainer, Mat. Sci. Eng. A - Struct, article under review.

[7] N. Winzer, A. Atrens, W. Dietzel, G. Song, K.U. Kainer, Mat. Sci. Eng. A - Struct **2007**, 466, 18.

[8] G. Song, A. Atrens, Adv. Eng. Mater. **1999**, 1, 11.

[9] G. Song, A. Atrens, Adv. Eng. Mater. **2003**, 5, 837.

[10] G. Song, A. Atrens, Adv. Eng. Mater. **2007**, 9, 177.

[11] A. Atrens, W. Dietzel, Adv. Eng. Mater. **2007**, 9, 292.

[12] S.P. Lynch, P. Trevena, Corrosion **1988**, 44, 113.

[13] E.I. Meletis, R.F. Hochman, Corrosion **1984**, 40, 39.

[14] D.G. Chakrapani, E.N. Pugh, Metall. Trans. A **1976**, 7, 173.

[15] A.J. Bursle, E.N. Pugh, in *Mechanisms of Environment Sensitive Cracking of Materials* (Eds: P.R. Swann, F.P. Ford, A.R.C. Westwood), Materials Society, London **1977**, 471.

[16] G.L. Makar, J. Kruger, K. Sieradzki, Corros. Sci. **1993**, 34, 1311.

[17] S.P. Lynch, Acta. Metall. **1988**, 34, 2639.

[18] S.P. Lynch, in *Hydrogen Effects on Material Behavior and Corrosion Deformation Interactions* (Eds: N.R. Moody, A.W. Thompson, R.E. Ricker, G.W. Was, R.H. Jones), TMS, Warrendale **2003**, 449.

[19] H.K. Birnbaum, in *Hydrogen Effects on Material Behavior* (Eds: N.R. Moody, A.W. Thompson), TMS, Warrendale **1990**, 639.

[20] J.K. Tien, R.J. Richards, Scripta Metall. **1975**, 9, 1097.

[21] W-Y. Chu, C-M Hsiao, S-Q. Li, Scripta Met. **1979**, 13, 1063.

[22] N.N. Kinaev, D.R. Cousens, A. Atrens, J Materials Science **1999**, 34, 4909.

[23] N.N. Kinaev, D.R. Cousens, A. Atrens, J Materials Science **1999**, 34, 4921.

[24] N.N. Kinaev, D.R. Cousens, A. Atrens, J Materials Science **1999**, 34, 4931.

[25] J. K. Tien, O. Buck, R. C. Bates, S. Nair, Scripta Met. **1980**, 14, 583.

[26] R.I. Stephens, C.D. Schrader, D.L. Goodenberger, K.B. Lease, V.V. Ogarevic, S.N. Perov, Society of Automotive Engineers, **1993**, 930752.

[27] M.O. Speidel, M.J. Blackburn, T.R. Beck, J.A. Feeney, Mechanics and Microstructure, NACE-2, **1972**, 324.

[28] K. Ebtehaj, D. Hardie, R.N. Parkins, Corros. Sci. **1993**, 28, 811.

[29] D.G. Chakrapani, E.N. Pugh, Metall. Trans. A **1975**, 6, 1155.

[30] W.R. Wearmouth, G.P. Dean, R.N. Parkins, Corrosion **1973**, 29, 251.

[31] S.Q. Shi, M.P. Puls, J. Nucl. Mater. **1994**, 208, 232.

[32] C. Yan, L. Ye, Y.-W. Mai, Materials Letters **2004**, 58, 3219.